

This is an electronic reprint of the original article. This reprint may differ from the original in pagination and typographic detail.

Boosting Perovskite Solar Cells Efficiency and Stability

Ding, Changzeng; Yin, Li; Wang, Jinlong; Larini, Valentina; Zhang, Lianping; Huang, Rong; Nyman, Mathias; Zhao, Liyi; Zhao, Chun; Li, Weishi; Luo, Qun; Shen, Yanbin; Österbacka, Ronald; Grancini, Giulia; Ma, Chang Qi

Published in:
Advanced Materials

DOI:
[10.1002/adma.202207656](https://doi.org/10.1002/adma.202207656)

Published: 31/10/2022

Document Version
Accepted author manuscript

Document License
All rights reserved

[Link to publication](#)

Please cite the original version:

Ding, C., Yin, L., Wang, J., Larini, V., Zhang, L., Huang, R., Nyman, M., Zhao, L., Zhao, C., Li, W., Luo, Q., Shen, Y., Österbacka, R., Grancini, G., & Ma, C. Q. (2022). Boosting Perovskite Solar Cells Efficiency and Stability: Interfacial Passivation of Crosslinked Fullerene Eliminates the "Burn-in" Decay. *Advanced Materials*, 35(2), Article 2207656. <https://doi.org/10.1002/adma.202207656>

General rights

Copyright and moral rights for the publications made accessible in the public portal are retained by the authors and/or other copyright owners and it is a condition of accessing publications that users recognise and abide by the legal requirements associated with these rights.

Take down policy

If you believe that this document breaches copyright please contact us providing details, and we will remove access to the work immediately and investigate your claim.

Boosting Perovskite Solar Cells Efficiency and Stability: Interfacial Passivation of

Crosslinked Fullerene Eliminates the “burn-in” Decay

Changzeng Ding, Li Yin, Jinlong Wang, Valentina Larini, Lianping Zhang, Rong Huang, Mathias Nyman, Liyi Zhao, Chun Zhao, Weishi Li, Qun Luo, Yanbin Shen, Ronald Österbacka, Giulia Grancini, Chang-Qi Ma**

Dr. Changzeng Ding, Dr. Qun Luo, Prof. Chang-Qi Ma

School of Nano-Tech and Nano-Bionics, University of Science and Technology of China,
398 Jinzhai Road, Hefei, 230026, P. R. China.

E-mail: cqma2011@sinano.ac.cn

Dr. Changzeng Ding, Lianping Zhang, Dr. Qun Luo, Prof. Ronald Österbacka, Prof. Chang-Qi Ma

This article has been accepted for publication and undergone full peer review but has not been through the copyediting, typesetting, pagination and proofreading process, which may lead to differences between this version and the [Version of Record](#). Please cite this article as [doi: 10.1002/adma.202207656](#).

This article is protected by copyright. All rights reserved.

i-Lab & Printable Electronics Research Center, Suzhou Institute of Nano-Tec and Nano-Bionics, Chinese Academy of Sciences (CAS), 398 Ruoshui Road, SEID, SIP, Suzhou 215123, P. R. China

Valentina Larini, Prof. Giulia Grancini

Department of Chemistry & INSTM, University of Pavia, Via T. Taramelli 14, 27100 Pavia, Italy

E-mail: giulia.grancini@unipv.it

Li Yin, Dr. Chun Zhao

School of Science, School of Advanced Technology, Xi'an Jiaotong-Liverpool University, 111 Renai Road, SEID, SIP, Suzhou 215123 China

Dr. Liyi Zhao, Prof. Yanbin Shen

i-Lab, Suzhou Institute of Nano-Tec and Nano-Bionics, Chinese Academy of Sciences

(CAS), 398 Ruoshui Road, SEID, SIP, Suzhou 215123, P. R. China

Jinglong Wang, Prof. Weishi Li

Shanghai Institute of Organic Chemistry, Chinese Academy of Science, 345 Lingling Road,

Shanghai 200032, P. R. China

Dr. Rong Huang

Vacuum Interconnected Nanotech Workstation, Suzhou Institute of Nano-Tec and Nano-

Bionics, Chinese Academy of Sciences (CAS), 398 Ruoshui Road, SEID, SIP, Suzhou

215123, P. R. China

Dr. Mathias Nyman, Prof. Ronald Österbacka

Physics and Center for Functional Materials, Faculty of Science and Technology, Åbo

Akademi University, Porthaninkatu 3, 20500 Turku, Finland

This article is protected by copyright. All rights reserved.

Abstract:

Perovskite solar cells (PSCs) longevity is nowadays the bottleneck for their full commercial exploitation. Although lot of research is ongoing, the initial decay of the output power – an effect known as “burn-in” degradation happening in the first hundred hours – is still unavoidable, significantly reducing the overall performance (typically of more than 20%). In this paper, we demonstrate the origin of the “burn-in” degradation in n-i-p type PSCs which is directly related to Li^+ ions migration coming from the SnO_2 electron transporting layer visualize by time-of-flight secondary ion mass spectrometry (ToF-SIMS) measurements. To block the ion movement, we introduced a thin crosslinked PC_{61}BM (CL-PCBM) layer on top of the SnO_2 layer, resulting in Li^+ immobilization. This resulted in the elimination of the “burn-in” degradation, showing for the first time a zero “burn-in” loss in the performances while boosting device PCE to > 22% for triple-cation based PSCs and > 24% for formamidinium-based (FAPbI_3) PSCs, proving the general validity of our approach and creating a new framework for the realization of stable PSCs devices.

Keywords: Perovskite solar cell, “burn-in” degradation, Li⁺ ions migration, crosslinked PCBM,

Operational stability

This article is protected by copyright. All rights reserved.

Introduction

Tremendous progress has been achieved in the field of perovskite photovoltaics in the last ten years, with certified PCE over 25.7%.^[1] Though surprising and remarkable progress, PSCs still suffer from unstable power output under the operation blocking their commercial uptake.^[2, 3] The instability comes from extrinsic degradation induced by humidity and/or oxygen,^[4] but also from intrinsic deterioration originating from multiple effects such as light-^[5] or bias-^[6] induced decomposition of perovskite layer, thermal-induced phase transition,^[7] electronic field-induced interface reactions or ions migration.^[8-10] While the extrinsic degradation can be avoided to a certain extent by carefully encapsulating the device,^[11-13] the intrinsic degradation paths can be mainly tackled by material, interfaces, and device optimization.^[14-16] Strategies include bulk and surface defect state passivation,^[17-19] interface engineering,^[20, 21] and importantly, control and inhibition of ion migration^[9]. However, despite a lot of research attention, severe degradation always manifests in the first hundred hours of operation, an effect called “burn-in” degradation, limiting the device stability.^[22-24] The “burn-in” degradation significantly reduces the overall power output of the cells (can be as large as 20%) and represents an obstacle in preserving the output efficiency. At present, the precise mechanisms behind such fast degradation are still unknown.^[24]

Previous research work relates “burn-in” degradation to ion migration in the perovskite layer and accumulation at the electron transport layer (ETL)/perovskite interface.^[25, 26] Few examples trying to reduce such effect include the work from Nazeeruddin *et al.* using a guanidinium (Gua)/Cs mixture in $\text{Cs}_x(\text{FAMAGua})_{1-x}$ perovskites to limit the bulk phase segregation and the associated burn-in decay,^[18] the work from Yu *et al.* using a modified- $\text{PC}_{61}\text{BM}/\text{SnO}_2$ passivating layer forming a more thermodynamically stable charge-transfer complex at the interface, which can inhibit the “burn-in” degradation.^[15] However, such device still suffer of partial initial degradation reducing the output power by 10%. The use of fullerene based modifiers has been widely explored to push n-i-p PSCs performances.^[27-30] However, the commonly used PC_{61}BM has a high solubility in organic solvents and thus can be easily washed away during deposition perovskite layer, with no control on the resulting layer.^[31, 32] In addition, the PC_{61}BM film tends to self-aggregate under illumination or thermal stress, as well as contributing in the delamination of the cell provoking severe instability.^[33]

In this work, we demonstrate the elimination of the “burn-in” degradation in highly efficient n-i-p PSCs by immobilizing the Li^+ ions migration from SnO_2 to the perovskite/hole transporting layer (HTL) interface, which we found being the main cause of it. To suppress it, we introduce a cross-linkable PC_{61}BM (CL- PC_{61}BM) as a functional interlayer in between the SnO_2 and the active perovskite layer. As a result, we demonstrate a push in the device

performances reaching 22.16% efficient triple cation-based and 24.19% formamidinium-based perovskite solar cells, with zero losses associated to the “burn-in” degradation, boosting the device stability.

Result and discussion

Interface engineering has been widely explored to enhance the efficiency and stability of PSCs.^[19] In particular, for n-i-p PSCs, defects at SnO₂ surface are responsible for a main decrease in the performance.^[27] To passivate them, fullerene derivatives have been the most popular materials used as surface modifiers ^[34-36]. In this work, we used two specific fullerene derivatives to modify the SnO₂ interfaces: [6,6]-phenyl-C₆₁-butyric acid methyl ester (PCBM) and a cross-linkable PCBM (CL-PCBM) (see **Figure 1a** for the molecular structures). **Figure 1b** shows the n-i-p PSCs structure with the PCBM and CL-PCBM films deposited on top of the SnO₂. The thickness of PCBM and CL-PCBM on SnO₂ before the deposition of perovskite film was measured to be 8.4 and 5.5 nm by atomic force microscope (AFM, **Figure S1** in supporting information). Crosslinking of CL-PCBM by thermal annealing was confirmed by the formation of insoluble byproducts, which is consistent with the differential scanning calorimetry (DSC) results.^[34] To prove the polymerization of CL-PCBM on SnO₂ surface upon thermal annealing at 200 °C, Fourier transform infrared spectroscopy

(FTIR) was performed on the CL-PCBM film on CaF_2 before and after thermal annealing.

The results are shown in **Figure S2**. Although IR signals for C=O and C-O can be clearly identified, the stretching vibration signal for C=C of the acrylate group ($\sim 1600 \text{ cm}^{-1}$) is too weak for comparison. To further confirm the success deposition of fullerene layer on SnO_2 , UV-vis absorption spectroscopy of the PCBM and CL-PCBM films before and after washing with DMF:DMSO mixed solvent were measured. As shown in **Figure S3** in supporting information, the absorbance of PCBM film decreased significantly after washing with the solvent, while the CL-PCBM film kept almost the same absorption to its initial value. These results indicate that the CL-PCBM film after thermal annealing showed improved solvent tolerance. In the full device case, the TOF-SIMS analysis (shown in **Figure S4**) verifies the formation of a carbon-rich layer on SnO_2 surface. In particular, a more intensive carbon signal is measured for the film with CL-PCBM interlayer with respect to standard PCBM demonstrating that a more condensed CL-PCBM layer formed on SnO_2 upon thermal-induced crosslinking of the fullerene derivatives. The surface morphology of PCBM and CL-PCBM deposited on SnO_2 was also characterized by scanning electron microscope (SEM) and atomic force microscope (AFM). As shown in **Figure S5** and **Figure S6**, the morphology of PCBM film changed after being washed by mixed solvent, whereas the morphology of CL-PCBM almost no change upon solvent treatment. The morphology results are in good

accordance with the UV-vis and SIMS results, confirming the successful deposition of CL-PCBM on SnO_2 .

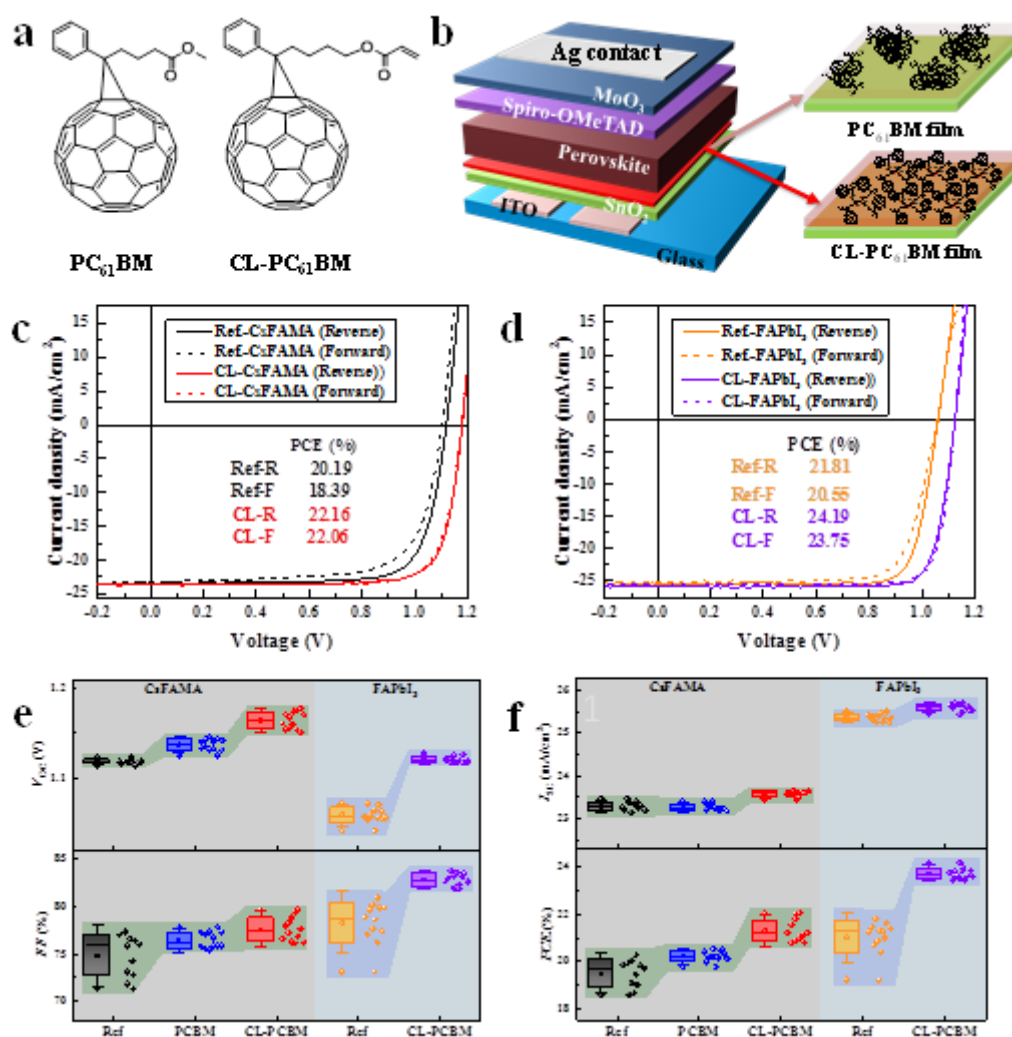


Figure 1. Chemical structure of the fullerene derivatives and the photovoltaic performances of the perovskite solar cells with different interfacial modification layers. (a) Chemical structures of

PC₆₁BM (PCBM) and cross-linkable PC₆₁BM (CL-PCBM). (b) Device structure with the different fullerene passivation thin film between the SnO₂ and perovskite layers. (c, d) $J-V$ curves of the CL-PCBM and reference PSCs based on CsFAMA (c) and FAPbI₃ (excess PbI₂ of 15%) (d) photoactive layers. (e, f) Comparison of the statistical V_{OC} and FF (e), J_{SC} , and PCE (f) of the solar cells with PCBM and CL-PCBM passivation layer to that of the reference cells (note: chemical compositions of the perovskite films are shown in the corresponding figure).

Table 1. Photovoltaic performance data of the PSCs deposited on various ETL

Perovskite	ETL	Scan direction	V_{oc} (V)	J_{sc} (mA/cm ²)	FF (%)	PCE (%)
CsFAMA	SnO ₂	Reverse	1.118	23.39	77.21	20.19
		Forward	1.101	23.22	71.92	18.39

FAPbI ₃	SnO ₂ /CL-	Reverse	1.178	23.63	79.67	22.16
	PCBM	Forward	1.176	23.62	79.44	22.06
	SnO ₂	Reverse	1.061	25.39	81.41	21.81
		Forward	1.057	25.31	76.80	20.88
	SnO ₂ /CL-	Reverse	1.125	25.66	83.80	24.19
	PCBM	Forward	1.124	25.60	82.54	23.75

Figure 1c and **1d** show the current density-voltage ($J-V$) curves of the best triple cations (CsFAMA) and formamidinium (FAPbI₃)-based PSCs upon different $J-V$ sweeping directions, respectively. The $J-V$ curves of the PCBM-based cells are shown in **Figure S7**. The distribution of the device parameters - open circuit voltage (V_{OC}) and fill factor (FF), short circuit current (J_{SC}), as well as the overall PCE are shown in **Figure 1e** and **1f**. The introduction of the fullerene interfacial layer while partially influencing the J_{SC} (see also the EQE spectra in **Figure S8**), significantly increases the V_{OC} and FF, leading to an overall PCE enhancement of ~10% after surface modification. Note that a slightly increased EQE at 680-750 nm was measured for the cell with CL-PCBM, which ensures a slightly higher J_{SC} for the CL-PCBM based cell. By checking with the layer thickness of the perovskite film (**Figure 2d-2f, vide infra**), we found that layer thickness of perovskite increases from 400 to 480 nm.

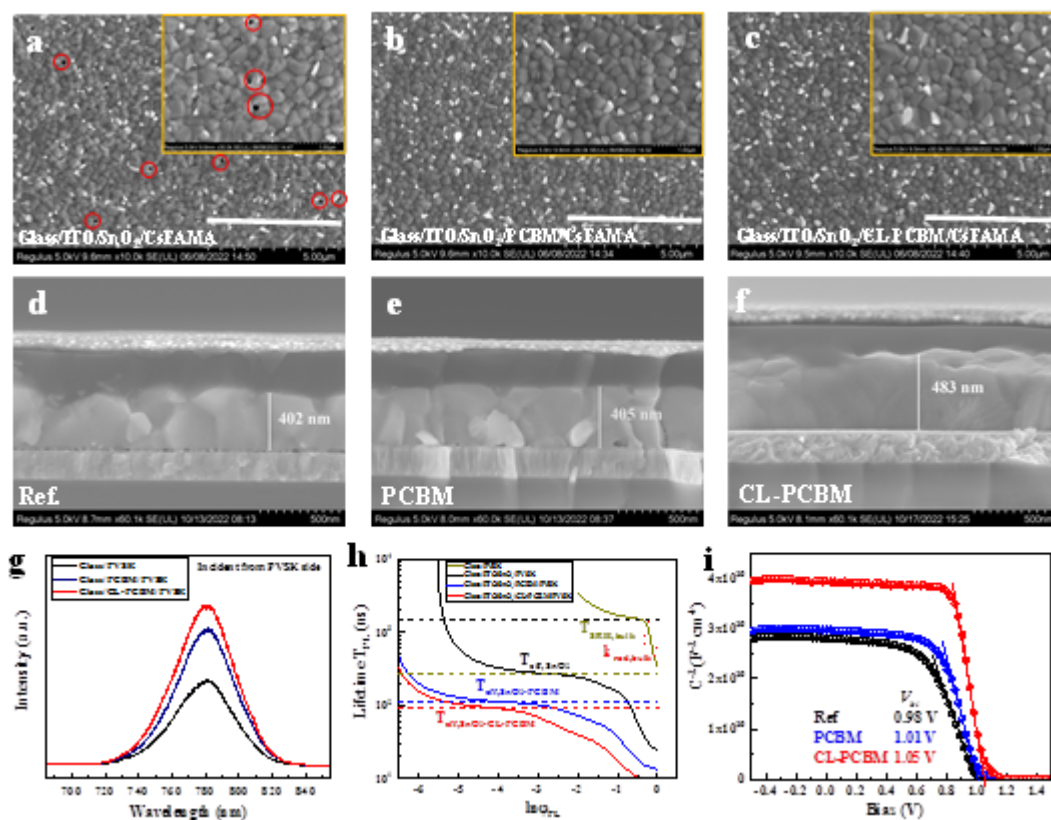
This is in good accordance with the UV-vis absorption spectra of these film (**Figure S9a**).

The numeric simulation revealed that shoulder absorption band shifts from 660 to 720 nm (**Figure S9b**), demonstrating that the increase EQE at 700 nm was mainly due to the optical effect originating from the increase of the perovskite thin film. The champion CsFAMA reference cell showed a PCE of 20.19%, with a J_{SC} of 23.39 mA cm⁻², a V_{OC} of 1.118 V, and an FF of 77.21%. The use of PCBM and CL-PCBM interfacial layer improves the PCE to 20.51% and 22.16%, respectively, mainly due to the increased V_{OC} (1.140 and 1.178) and FF (77.31% and 79.67%, **Figure 1c** and **S7**). Compared with PCBM, the CL-PCBM-based cells showed higher device performance, suggesting a better surface passivation effect of the CL-PCBM layer, which can be attributed to the more condensed CL-PCBM film on SnO₂ after crosslinking in agreement with the TOF-SIMS analysis (**Figure S4**). Similarly, improved V_{OC} (1.125 V vs. 1.061 V) and FF (83.80% vs. 81.41%) yield enhanced the PCE reaching 24.19% (vs. 21.81%) for the CL-PCBM-based FAPbI₃ cells (**Figure 1d**). The photovoltaic performance data are summarized in **Table 1**. FAPbI₃-based PSCs using aluminum (Al) as the top metal electrode were also fabricated and tested. **Figure S10** showed the $J-V$ curves and the statistical photovoltaic performance data of the cells compared to the reference cells. Although the Al-based cells showed lower PCE than the corresponding Ag-based cells

(22.39% vs. 24.19%), the better surface passivation effect of the CL-PCBM layer can still be confirmed (22.39% vs. 20.50%, **Figure S10**), confirming the validity of our findings.

To better investigate the origin of such improvement in the device performances we further characterize the morphology and the crystal quality of the perovskite layer deposited on top of the modified interface. **Figure 2a to 2c** display the scanning electron microscopy (SEM) images of CsFAMA perovskite crystals deposited on SnO_2 , SnO_2/PCBM , and $\text{SnO}_2/\text{CL-PCBM}$, respectively. Nano-sized pinholes (marked in circles) are visible between some grains in perovskite film deposited on SnO_2 . On the other hand, the morphology of the perovskite on top of PCBM/CL-PCBM modifications is more compact with no observable pinholes, showing the better quality of perovskite crystals. In addition, the cross-section images of the solar cells with different ETLs, as shown in **Figure 2d-2f**, revealed that pinholes are formed at the SnO_2 /perovskite interface, whereas less pinholes were found at the SnO_2/PCBM /perovskite. For the CL-PCBM modified cell, the pinholes at the interface of $\text{SnO}_2/\text{CL-PCBM}$ /Perovskite were fully eliminated and a compact interface was formed. Also, the introduction of CL-PCBM layer yield a thickner perovskite film with a thickness of 480 nm. The results indicates that the CL-PCBM modification is beneficial to reduce the defects at the interface of ETL/Perovskite and form a thicker perovskite film. The Dark $J-V$ curves of the electron-only devices with and without PCBM/CL-PCBM passivation layer showed a

higher injection current at high voltage (**Figure S11**), indicating a better interface for the fullerene incooperated cells. The crystallinity of FAPbI₃ perovskite films deposited on SnO₂ and SnO₂/CL-PCBM substrate was also tested by SEM (**Figure S12a and S12b**), and results show an improved thin film quality of the FAPbI₃ film on CL-PCBM. Knowing that the crystallinity of the perovskite film is sensitive to the surface's wettability, we attribute the improvement the perovskite film to the hydrophobic property of the fullerene layer. The similar passivation effect of CL-PCBM was also found in dark $J-V$ curves of electron-only devices, as shown in **Figure S12c**.



This article is protected by copyright. All rights reserved.

Figure 2. SEM images, Steady state photoluminescence (PL), space charge-limited current (SCLC) and Mott-Schottky (M-S) curves based on CsFAMA PSCs with different ETLs. The SEM images of (a) SnO₂, (b) SnO₂/PCBM and (c) SnO₂/CL-PCBM based CsFAMA perovskite films. The cross-sectional images of (d) Ref. (e) PCBM and (f) CL-PCBM modified cells. (g) PL spectra of perovskite film deposited on Glass, Glass/PCBM and Glass/CL-PCBM substrate. (h) Differential lifetime as a function of the logarithm of the TRPL intensity, which serves as a relative measure of the quasi-Fermi level splitting, $\ln(\phi_{PL}) \propto \Delta E_F$. The plateau of τ_{PL} seen for the pristine perovskite sample was used to estimate the Shockley Read Hall (SRH) lifetime $\tau_{SRH,bulk}$ in the bulk. (i) M-S curves of the reference, PCBM, and CL-PCBM based cells.

The steady-state photoluminescence (PL) and time-resolved photoluminescence (TRPL) measurements are then carried out to study the effect of ETLs on crystallinity of the CsFAMA perovskite and the interfacial charge dynamics of ETL/Perovskite. **Figure 2g** reports the photoluminescence (PL) spectra of the perovskite film deposited on the different surfaces. As seen there, more intensive PL was measured for the perovskite films deposited on Glass/PCBM and Glass/CL-PCBM surfaces, suggesting a less nonradiative recombination within the film with CL-PCBM, which can be ascribed to the increase the crystalline quality and the improved interface connection (**Figure 2a-2f**). Which also indicate the decreased nonradiative recombination in the perovskite layer.

To distinguish the effect of bulk and interface after PCBM/CL-PCBM modification, the TRPL of perovskite film deposited on ITO substrate with different ETLs was characterized, results are shown in **Figure S13**. It has proved the traditional used exponent lifetime could not distinguish the effects in bulk and at the interface, a differential lifetime can help to distinguish these effects.^[37, 38] The detail of differential lifetime of TRPL results can be found in Supporting information. In **Figure 2h**, the plateau of τ_{PL} for the samples with ETL is in this case given by a complex interplay of the bulk SRH lifetime and the surface recombination velocity S (Here, we assumed the energy level offset at the interface is negligible). Hence, the surface recombination velocity S can be calculated with the following equation and the related results are shown in **Table S3**.

$$\tau_{SRH,eff} = \left(\frac{1}{\tau_{SRH,bulk}} + \frac{S}{2d} \right)^{-1}$$

Where d is the thickness of the perovskite layer, which can be found in **Figure 2d-2f**. Hence, the CL-PCBM passivation layer could increase S from 246 to 975 cm/s, indicating that the majority carriers will experience a better extraction through that interface.

On the other side, aiming at elucidating the charge transporting/recombination dynamics at the ETL/perovskite interfaces, we performed the Mott-Schottky (M-S) test on different PSCs. **Figure 2i** depicts the M-S diagram of reference, PCBM and CL-PCBM cells.

Assuming a uniformly doped in the perovskite layer, and that the highly conductive Spiro-OMeTAD and SnO₂ layers act as extensions of the contacts, the measured capacitance C relates to the applied potential V as $C^{-2} = 2(V_{bi} - V) / (A^2 q \epsilon \epsilon_0 N_d)$,^[39] where ϵ is the static permittivity (~62 for CsFAMA perovskite material)^[40], ϵ_0 is the permittivity of free space, A is the active area of the devices, q is the elementary charge, N_d is the doping density, and V_{bi} is the built-in potential. V_{bi} was determined from the intersection of the tangent of the linear part of the Mott-Schottky plots with the x-axis. The pristine SnO₂-based PSCs exhibited a V_{bi} of 0.98 V, whereas the PCBM- and CL-PCBM-based PSCs exhibited an enhanced V_{bi} of 1.01 V and 1.05 V. Enhancing the V_{bi} has previously been shown to improve device performance, in particular the V_{oc} , explaining the V_{oc} enhancement obtained.^[41] The perovskite layer is moderately doped with similar doping densities; the doping density (N_d) of three devices can be extracted to be 8.1×10^{16} , 1.1×10^{17} , 1.8×10^{17} cm⁻³ for the reference, PCBM- and CL-PCBM-based PSCs, respectively. In FAPbI₃ cells, the V_{bi} was also improved from 1.00 V to 1.06 V, upon SnO₂ surface modification with CL-PCBM (**Figure S12d**), corresponding to an increased doping density (N_d) from 8.45×10^{16} to 1.44×10^{17} cm⁻³, again demonstrating the similar surface passivation effect of the CL-PCBM layer. One should note that although the initial layer thicknesses of PCBM and CL-PCBM were around 8.4 and 5.5 nm (*vide supra*), layer thickness of PCBM should be significantly reduced owing to the

solvent washing effect, while CL-PCBM should have a layer thickness around 5 nm for its more robust against solvent (**Figure S3**). Assuming the C signal intensity in SIMS is proportional to the layer thickness, the yield PCBM layer is estimated to be 1.1 nm, that is 1/5 of CL-PCBM layer (**Figure S4**). Considering the layer thickness of perovskite is around 400 nm, the influence of the layer thickness of PCBM and CL-PCBM on the capacitance of the cells is neglectable. However, a thicker perovskite layer for CL-PCBM based cell significantly influence the capacitance of the cells, yielding a higher C^{-2} in **Figure 2f**.

How the interfacial modification relates to device stability is pivotal to understand. While it is common knowledge that n-i-p type PSCs using SnO_2 as ETL and Li-doped Spiro-OMeTAD as hole transport layer (HTL) show excellent photovoltaic performance, they are often affected by severe losses in device stability which poses severe constraints on the device operation in real conditions.^[20, 22, 42] This is mainly due to shunting paths originating from the formation of conductive filament that originated from the ions migrations in the Spiro-OMeTAD layer.^[43] Inserting buffer layers such as MoO_3 can be a partial solution to that, simultaneously preventing the oxidation of the silver electrode, creating a smooth thin film, and blocking the holes generated in the cells. However, significant “burn-in” performance decay, which means a loss in the performance up to 20% in the first few hours of operation - affects this PSC architecture (**Figure 3a**), while remaining stable on longer

times. A typical $J-V$ curve of the cell is shown in **Figure S14**. The PCE decay can be fitted by a bi-exponential decay model, from which we retrieve the first decay of 4.6 h and the second one of 155.4 h, see **Figure 3a**. Clearly, the rapid “burn-in” degradation at the first stage is responsible for this overall severe performance decay. Monitoring more in details the continuous operation over 6000 s, the reference, PCBM and CL-PCBM devices retained 85%, 90%, and 95% of initial PCE (**Figure 3b** and **Figure S15**), respectively. Indicating that the CL-PCBM modification can effectively improve the stability of PSCs. We study the “burn-in” decay process more in details during the operational stability test in the first few hours, by performing a continuous current density-voltage ($J-V$) scan (see **Figure S16**) and again after storing the cell in the dark for 60 s. A reversible “burn-in” decay is observed.^[26] Indicating that reversible ion migrations are mostly involved in the “burn-in” degradation process (see details in **Figure S17**).

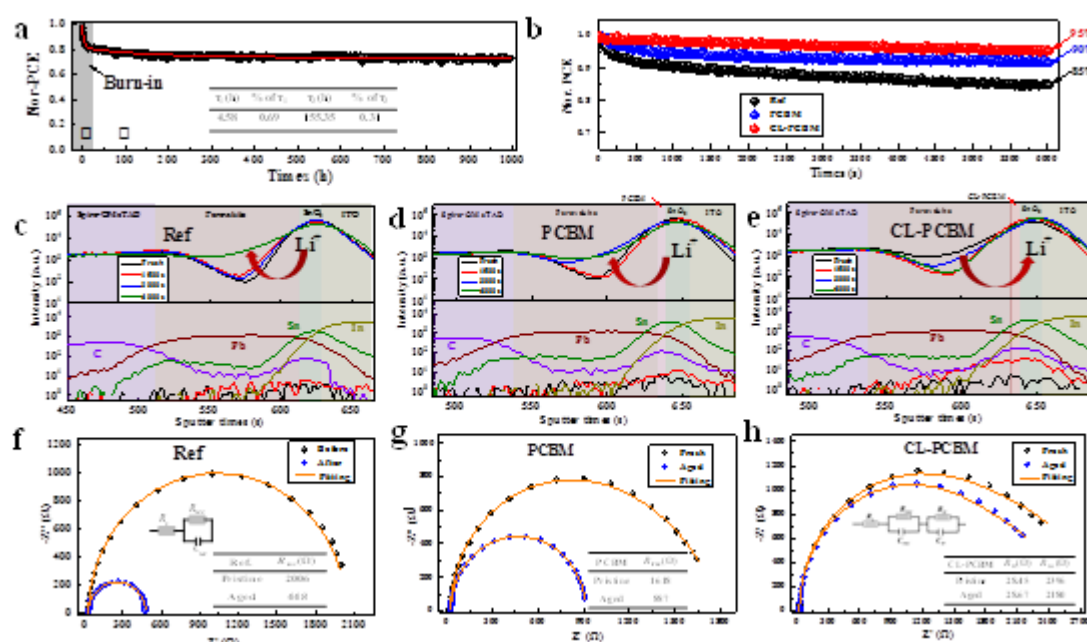


Figure 3. (a) The long-term operational stability curves of ref. cells under MPP tracking with continuous illumination. (b) Evolution of the PCE of PSCs under continuous light illumination with Li-TFSI doped Spiro-OMeTAD as HTL and SnO₂, SnO₂/PCBM and SnO₂/CL-PCBM as ETL, respectively. Li⁺ ions profiles and EIS of solar cells. Li⁺ ion profiles test by ToF-SIMS based on (c) Reference, (d) PCBM and (e) CL-PCBM devices. EIS spectrum and fitting results of (f) Reference, (g) PCBM and (h) CL-PCBM devices.

To better understand the phenomena behind the “burn-in” degradation, we performed the ToF-SIMS measurement to monitor the depth profiles of the Li⁺ ions soon after $J-V$ sweeping for different times (see **Figure 3c to 3e**). The element distribution profiles for the

pristine cells were also measured for comparison. For all these three pristine cells, much higher Li^+ concentration was measured in the SnO_2 layer than in the Spiro-OMeTAD layer. These findings are similar to our previous report, and the higher Li^+ concentration in the SnO_2 layer was ascribed to the migration of Li^+ ions during the deposition and oxidation of Spiro-OMeTAD layer.^[44] In the case of reference cells with bare SnO_2 ETL, diffusion of Li^+ ions into the perovskite layer happens after a continuous operational stability test, which may change the charge transport and extraction efficiency. Besides Li^+ ions migration, the I^- ions were also easily migrated during the operation of the cells.^[26, 45] However, the I^- ions profile does not show any changes during the continuous J/V scanning test, as seen in **Figure S18**, which indicates the migration of I^- ions does not cause the “burn-in” degradation process. To further explore this behavior, we measured the electric impedance spectroscopy (EIS) of the cells before and after the operational stability test at V_{OC} and in the dark. **Figure 3f** shows the Nyquist plots and the numerical fitting results according to the equivalent circuit shown in **Figure 3f**. In the EIS analysis, the high-frequency component is the signature of the transfer resistance (R_{tr}) and the low-frequency is for the recombination resistance (R_{rec}).^[46] The R_{tr} of the pristine device was found to be rather stable over J/V sweeping (33.51 vs. 32.19 Ω), indicating the electron extraction is not affected upon aging. However, the recombination resistance R_{rec} decreased significantly from 2006 Ω to 448 Ω . This means the charge

recombination at the interface is increased owing to the accumulation of Li^+ ions. We then measured the Li^+ distribution and charge recombination resistance of the PCBM and CL-PCBM modified cells by TOF-SIMS and EIS, respectively. **Figure 3d – 3e** and **Figure 3g – 3h** show the Li^+ ions distribution and EIS of the PCBM and CL-PCBM modified devices, respectively. For the PCBM modified device, Li^+ ions migration from the SnO_2 layer into the perovskite layer was also found. And the R_{rec} was decreased from $1618 \, \Omega$ to $887 \, \Omega$ for the cell after $J-V$ sweeping, suggesting the increased charge recombination rate after aging. For the CL-PCBM modified cell, however, decreased Li^+ ion concentration was measured in the perovskite layer for the cell after age, whereas R_{rec} measured from EIS was slightly decreased from $2396 \, \Omega$ to $2180 \, \Omega$. Note that slight “burn-in” degradation was measured for the PCBM modified cells, while almost no “burn-in” degradation was measured for the CL-PCBM cell (**Figure 3b**). These results indicate that fullerene derivatives can immobilize Li^+ within the cell and CL-PCBM exhibits a better immobilization effect. To verify the SnO_2 and PCBM can immobilize Li^+ ions in the cell, we utilized SnO_2 and PCBM as the cathode for room-temperature Li-ion batteries. The galvanic discharge-charge (GDC) voltage profiles of both batteries were measured and the results are shown in **Figure S19**. As seen here, both SnO_2 and PCBM have good Li^+ ions storage capacity during discharge process. However, during the charging process, in $\text{Li} \parallel \text{SnO}_2$ cell, the delithiation is more likely to occur, while in

Li || PCBM cell, only a small part of Li^+ ions in PCBM was removed. This indicating that PCBM has excellent capability to immobilize Li^+ ions. Recently, Qiu *et al.* reported that owing to the excellent electrochemical reaction of C_{60} , lithiation/delithiation can be formed during the charge-discharge process, and form fulleren-lithium adducts.^[47-49] Since CL-PCBM has similar conjugated molecular core unit as PCBM, the Li^+ storage mechanism of CL-PCBM should be similar to PCBM. The measured Li^+ ions migration behavior is in good accordance with the “burn-in” decay of the cells, which indicates Li^+ ions migration from SnO_2 to the perovskite and spiro-OMeTAD layer is the main reason for the “burn-in” degradation of the cell.

To further confirm that Li^+ ions migration is involved in the fast “burn-in” degradation, we fabricated n-i-p type perovskite solar cells using P3HT instead of Spiro-OMeTAD layer as the HTL (see experiment part and **Figure S20-S22**). The Li^+ doped SnO_2 device using and P3HT as HTL manifests the “burn-in” PCE decay (around 20%), whereas after depositing a crosslinked CL-PC₆₁BM, the “burn-in” decay process is significantly inhibited. This result strongly confirms that the Li^+ ions in the SnO_2 layer are a key factor causing the “burn-in” degradation. This is further supported by additional ToF-SIMS (**Figure S22b** and **S22c**) analysis. For the Li^+ ions contained devices (device B and C in **Figure S20**), Li^+ ions are found to be mainly located at the perovskite/ SnO_2 and perovskite/CL-PCBM/ SnO_2 interfaces.

The accumulation of Li^+ ions at the perovskite/P3HT interface was also detected, which can be ascribed to the Li^+ ion migration from $\text{SnO}_2:\text{Li}^+$ to the HTL. Upon aging, Li^+ ion concentration at the interface of Perovskite/P3HT increased in device B, in good accordance with the measured “burn-in” decay of device (**Figure 3c**). Differently, after introducing CL-PCBM, the Li^+ ions concentration at the perovskite/P3HT interface decreased after aging (**Figure S22c**). All these results prove that the migration of Li^+ ions from SnO_2 to the interface of perovskite/HTL could be the reason resulting in “burn-in” degradation, whereas the CL-PCBM can immobilize the Li^+ ions in SnO_2 and consequently minimize the “burn-in” performance degradation. During the operation of the cells, the Li^+ ions concentrate at the interface of HTL/Perovskite, which increases the charge recombination and decreases the device performance. Although our results showed also the interface connection between SnO_2 and perovskite was improved by introducing a thin fullerene layer, which is beneficial to the stability of the cells, the migration of Li^+ during the aging is ascribed to the fundamental chemical reason for the “burn-in” degradation according to the results described above.

Finally, the long-term operational stability of PSCs is investigated. **Figure 4a** shows the PCE evolution of a typical CsFAMA-based PSC with or without CL-PCBM interfacial layer having initial PCE of 19.70% and 22.03%, respectively (see **Figure S23** and **Figure S24**). As

seen here, the reference cell shows a rapid “burn-in” degradation in the first 20 h, which led to an overall 20% PCE decay. After being modified by CL-PCBM, the burn-in degradation was inhibited. The CL-PCBM-based device retains 95% of initial efficiency after aging over 1000 h, demonstrating the simultaneous performance and stability improvement effect of the CL-PCBM layer. Note that the PCBM based cells showed also “burn-in” decay upon long time aging (**Figure S25**), which could be due to the lower layer thickness of PCBM layer owing to the washing effect during the deposition of perovskite layer (vide supra, **Figure S3** and **S4**).

Similarly, we tested the long-term operational stability of high-performance FAPbI₃-based PSCs with Ag top electrode (see also **Figure S26** and statistics in **Figure S27**). As shown in **Figure 4b**, the CL-PCBM layer containing devices showed improved operational stability with zero losses at initial times. After aging for 980 h, the cell with CL-PCBM modification retained the initial PCE of 92%, which are higher than that of the reference cells which decreases for about 25%, clearly demonstrating the stabilization effect of CL-PCBM, the statistical stability data is shown in **Figure S28**. Results are also confirmed using Al-based electrodes (**Figure S29**).

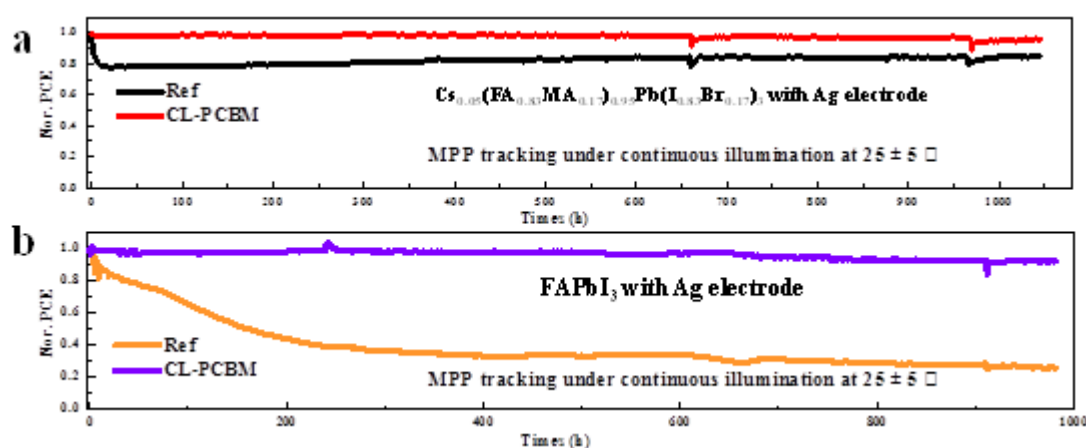


Figure 4. Operational stability of PSCs under MPP tracking with continuous illumination at 25 ± 5°C, (a) CsFAMA-based and (b) FAPbI₃-based solar cells with Ag top electrode.

In conclusion, we demonstrated that Li⁺ ions migration from the SnO₂ surface to the perovskite/HTL interface is responsible for the “burn-in” degradation of the n-i-p type of perovskite solar cells. The decreased Li⁺ concentration at the perovskite/SnO₂ interface and the increased Li⁺ concentration at the HTL/perovskite interface simultaneously lower the charge extraction efficiency and increase the charge recombination, and consequently decrease device performance. A thin cross-linked fullerene layer (CL-PCBM) forming a uniform surface passivation layer is used to block such movement. As a result, it induces the immobilizing the Li⁺ ions at the SnO₂ layer reducing charge recombination but it also eliminates the built-in degradation of the cell, synergistically resulting in higher device performance and boosted stability. The current work provides a deep understanding of the

“burn-in” degradation process of PSCs, which stems true independently from the composition of the active perovskite layer, providing a new direction for demonstrated efficient and stable solar cells.

Experimental Section

Materials:

The SnO₂ colloid solution was purchased from Alfa Aesar (tin (IV) oxide, 15 wt% in H₂O colloidal dispersion). [6,6]-phenyl-C61-butyric acid methyl ester (PC₆₁BM) was purchased from Sigma-Aldrich, crosslink PC₆₁BM (CL-PC₆₁BM) was synthesized by the method in literature.^[34] Pbl₂, PbBr₂, CsI, Formamidinium iodide (FAI), methylammonium bromide (MABr), n-Octylammonium Iodide (OAI), Lithium bis(trifluoromethanesulphony)imide (LiTFSI), Pyridine,4-(1,1-dimethylethyl)- (t-BP) and Spiro-OMeTAD were purchased from Xi'an Polymer Light Technology Corp`, dimethylformamide (DMF, purity>99%), dimethyl sulfoxide (DMSO, purity>99%), chlorobenzene (CB, purity>99%) and isopropanol (IPA, purity>99%)were purchased from J&K scientific. All materials were used directly.

Instruments and characterization

The current density-voltage ($J-V$) characters of solar cells were measured with a Keithley 2400 source meter in an N₂ glove box under a simulated sun AM 1.5 G (Newport VeraSol- 2 LED Class AAA Solar Simulator). The EQE of each cell was measured using a home-made IPCE system consisting of a 150W tungsten halogen lamp (Osram 64642), a monochromator (Zolix, Omni-I300), an optical chopper, and an I-V converter (QE-IV Convertor, Suzhou D&R Instruments) equipped with lock-in amplifier (Stanford Research Systems SR 830). To better simulate the device under 1 sun condition, bias light from a 532 nm solid-state laser was introduced to the cell simultaneously. A calibrated Si solar cell was used as a reference. SEM images were gained by a field-emission scanning electron microscope (S-4800) under an accelerating voltage of 5 kV. The time-of-flight secondary ion mass spectrometry (TOF-SIMS 5-100) was measured with the pulsed primary ions from a Cs⁺ (2 keV) liquid-metal ion gun for sputtering and a Bi⁺ pulsed primary ion beam for analysis (30 keV). Electrical impedance spectroscopy (EIS) and Mott-Schottky (M-S) measurements were carried out on the electrochemical workstation (PGSTA302N). The EIS measure conditions were under dark and applied bias at open voltage, the frequency range is 0.1 Hz-10 MHz. The M-S plot measurement conditions were determined to be a 10 kHz frequency.

Preparation of the solutions

The SnO₂ colloid solution (15 wt%) was diluted using deionized water to the concentration of 3 wt%. Then, the solution was stirred at room temperature for 2 h.

PC₆₁BM and CL-PC₆₁BM solution: 3 mg of PC₆₁BM and CL-PC₆₁BM were dissolving in 1 mL CB, stirring at room temperature for 2 h. The Cs_{0.05}(FA_{0.85}MA_{0.15})_{0.95}Pb(I_{0.85}Br_{0.15})₃ (CsFAMA) precursor solution was prepared by dissolving PbI₂ (548.6 mg), PbBr₂ (77.07 mg), FAI (190.12 mg), and MABr (21.84 mg) in a mixture solvent of DMF/DMSO (1 mL. 4:1 v/v). Then, 34 µL CsI (2 M in DMSO) was added to a mixed perovskite solution, stirring for 2 h at room temperature. The FAPbI₃ precursor solution (1.5 M) was prepared by dissolving PbI₂ 795.24 mg (excess 15%) or 726.09 mg (excess 5%), FAI 257.96 mg, MACI 35 mg and DMACI 3.4 mg in a mixture solvent of DMF/DMSO (1 mL. 4:1 v/v), stirring for 2 h at room temperature. The OAI solution was prepared by dissolving 5 mg OAI into 1 mL IPA, stirring for 2 h at room temperature. The Spiro-OMeTAD solution was prepared by dissolving 72.3 mg Spiro-OMeTAD into 1 mL chlorobenzene followed by the addition of 17.5 µL Li-TFSI (520 mg/mL in acetonitrile) and 29 µL t-BP, this solution was stirred overnight at room temperature.

Solar cell fabrication

ITO glass was cleaned by ultrasonic cleaning through detergent, and pure water was dried by N₂ gas flow, and cleaned by UV Ozone for 30 min. Then the substrate was spin-coated

with a thin layer of SnO₂ nanoparticle from the SnO₂ colloid solution at 3000 rpm for 30 s, and annealed in ambient air at 150 °C for 30 min. then the SnO₂ film was further treated by UV Ozone for another 10 min. For the PC₆₁BM and CL-PC₆₁BM layer was prepared in N₂ glovebox, 30 µL of PC₆₁BM and CL-PC₆₁BM was dipped on SnO₂ film and spin-coated at 5000 rpm for 30 s, and then annealed at 200 °C for 30 min. The Perovskite precursor solution was spin-coated on the SnO₂ and PC₆₁BM/CL-PC₆₁BM substrate.

For the CsFAMA perovskite films, the spin-coated process was divided by a consecutive two-step process, the spin rate of the first step is 2000 rpm for 10 s with an accelerated speed of 500 rpm, and the spin rate of the second step is 6000 rpm for 20 s with an accelerated speed of 1000 rpm. During the second step end of 10 s, 200 µL of ethyl acetate was drop-coated to treat the perovskite films, and then the perovskite films were annealed at 120 °C for 45 min in a glovebox.

For the FAPbI₃ perovskite films were spin-coated at 5000 rpm for 30 s with an accelerated speed of 1000 rpm, during the end of 10 s, 200 µL of chlorobenzene was drop-coated to treat the perovskite films, and then the perovskite films were annealed at 150 °C for 30 min in a glovebox.

After cooling down to room temperature, the OAI solution was coated on perovskite films at 5000 rpm for 30s. Then, the spiro-OMeTAD solution was coated on perovskite films at 3000 rpm for 30 s with an accelerated speed of 3000 rpm. After that, the Spiro-OMeTAD layer was fully oxidized in the air with a humidity of 30% for 5 h.

After the oxidation process, a fully covered MoO_3 was deposited on spiro-OMeTAD by thermal evaporation with a rate of 0.2 nm/s, with a thickness of 10 nm. Then, a structured Ag electrode was deposited on the MoO_3 layer with a rate of 0.5 nm/s, and a thickness of 150 nm. For the Al based cells, a thickness of 150 nm Al was deposited on MoO_3 with a rate of 2 nm/s.

Operation stability test

Operation stability of the cells was performed on a multi-channel solar cell performance decay testing system ((PVL-T-G8001M, Suzhou D&R Instruments Co. Ltd.) inside a N_2 -filled glove box ($\text{H}_2\text{O} < 10$ ppm, $\text{O}_2 < 10$ ppm), and the cells were illuminated with a white LED light (D&R Light, L-W5300KA-150, Suzhou D&R Instruments Co. Ltd.) at a simulated one sun intensity (the initial short current equals to the J_{SC} measured under standard condition). The cell's performance was measured by I - V sweeping from 1.2 V to -0.05 V, with a step of 0.01 V. The temperature was set at 25 °C. Current density-voltage (J - V) characteristics of the

cells were measured periodically, and the maximum power output point (mpp) was calculated automatically. An external resistor that matches the mpp point ($R = I_{\max}/V_{\max}$) was then attached to the cells in between $J-V$ sweepings according to the $J-V$ sweeping results so that the recorded PCE decay curves directly reflect the performance decay of the cells under the simulated operational situation.

Acknowledgments

The authors would like to acknowledge the financial support from the Chinese Academy of Science (No.YJKYYQ20180029), Jiangsu Science and Technology Program (BE2022021, BE2022023), Suzhou Science and Technology Program (ST202219), Ministry of Science and Technology Project (G2021014029L), and the “Green flexible hybrid perovskite solar module for the market: from smart lead manipulation to recycling (FLHYPER)” project, funded under the “Circular Economy-2020” call. We would also like to thank the technical support for Nano-X from Suzhou Institute of Nano-Tech and Nano-Bionics, Chinese Academy of Science (No. A2107). G.G. acknowledges the “HY-NANO” project that received funding from the European Research Council (ERC) Starting Grant 2018 under the European Union’s Horizon 2020 research and innovation program (Grant Agreement No. 802862).

Reference

- [1] <https://www.nrel.gov/pv/cell-efficiency.html>, (accessed: December 2021).
- [2] K. Domanski, E. A. Alharbi, A. Hagfeldt, M. Grätzel, W. Tress, *Nat. Energy* **2018**, 3, 61.
- [3] M. V. Khenkin, E. A. Katz, A. Abate, G. Bardizza, J. J. Berry, C. Brabec, F. Brunetti, V. Bulovic, Q. Burlingame, A. Di Carlo, R. Cheacharoen, Y. B. Cheng, A. Colmann, S. Cros, K. Domanski, M. Dusza, C. J. Fell, S. R. Forrest, Y. Galagan, D. Di Girolamo, M. Graetzel, A. Hagfeldt, E. von Hauff, H. Hoppe, J. Kettle, H. Koebler, M. S. Leite, S. Liu, Y. L. Loo, J. M. Luther, C. Q. Ma, M. Madsen, M. Manceau, M. Matheron, M. McGehee, R. Meitzner, M. K. Nazeeruddin, A. F. Nogueira, C. Odabasi, A. Osherov, N. G. Park, M. O. Reese, F. De Rossi, M. Saliba, U. S. Schubert, H. J. Snaith, S. D. Stranks, W. Tress, P. A. Troshin, V. Turkovic, S. Veenstra, I. Visoly-Fisher, A. Walsh, T. Watson, H. B. Xie, R. Yildirim, S. M. Zakeeruddin, K. Zhu, M. Lira-Cantu, *Nature Energy* **2020**, 5, 35.
- [4] C. C. Boyd, R. Cheacharoen, T. Leijtens, M. D. McGehee, *Chem. Rev.* **2019**, 119, 3418.
- [5] Y. Jiang, S.-C. Yang, Q. Jeangros, S. Pisoni, T. Moser, S. Buecheler, A. N. Tiwari, F. Fu, *Joule* **2020**, 4, 1087.

-
- [6] M. V. Khenkin, A. K. M., E. A. Katz, I. Visoly-Fisher, *Energy Environ. Sci.* **2019**, 12, 550.
- [7] J. A. Steele, M. Lai, Y. Zhang, Z. Lin, J. Hofkens, M. B. J. Roefsaers, P. Yang, *Acc. Mater. Res.* **2020**, 1, 3.
- [8] S. Tan, I. Yavuz, N. D. Marco, T. Huang, S.-J. Lee, C. S. Choi, M. Wang, S. Nuryyeva, R. Wang, Y. Zhao, H.-C. Wang, T.-H. Han, B. Dunn, Y. Huang, J.-W. Lee, Y. Yang, *Adv. Mater.* **2020**, 32, 1906995.
- [9] Y. Zhao, W. Zhou, Z. Han, D. Yu, Q. Zhao, *Phys.Chem.Chem.Phys.* **2021**, 23, 94.
- [10] S. Ghosh, R. Singh, A. S. Subbiah, P. P. Boix, I. M. Seró, S. K. Sarkar, *Appl. Phys. Lett.* **2020**, 116, 113502.
- [11] S. Ma, G. Yuan, Y. Zhang, N. Yang, Y. Li, Q. Chen, *Energy Environ. Sci.* **2022**, 15, 13.
- [12] S. Ma, Y. Bai, H. Wang, H. Zai, J. Wu, L. Li, S. Xiang, N. Liu, L. Liu, C. Zhu, G. Liu, X. Niu, H. Chen, H. Zhou, Y. Li, Q. Chen, *Adv. Energy Mater.* **2020**, 10, 1902472.
- [13] L. Shi, M. P. Bucknall, T. L. Young, M. Zhang, L. Hu, J. Bing, D. S. Lee, J. Kim, T. Wu, N. Takamure, D. R. McKenzie, S. Huang, M. A. Green, A. W. Y. Ho-Baillie, *Science* **2020**, 368, 1328.

-
- [14] Q. Lou, Y. Han, C. Liu, K. Zheng, J. Zhang, X. Chen, Q. Du, C. Chen, Z. Ge, *Adv. Energy Mater.* **2021**, 11, 2101416.
- [15] P. Hang, J. Xie, C. Kan, B. Li, Y. Zhang, P. Gao, D. Yang, X. Yu, *Adv. Mater.* **2021**, 33, 2006910.
- [16] F. Zhang, S. Y. Park, C. Yao, H. Lu, S. P. Dunfield, C. Xiao, S. Uličná, X. Zhao, L. D. Hill, X. Chen, X. Wang, L. E. Mundt, K. H. Stone, L. T. Schelhas, G. Teeter, S. Parkin, E. L. Ratcliff, Y.-L. Loo, J. J. Berry, M. C. Beard, Y. Yan, B. W. Larson, K. Zhu, *Science* **2022**, 375, 71.
- [17] J. Jeong, M. Kim, J. Seo, H. Lu, P. Ahlawat, A. Mishra, Y. Yang, M. A. Hope, F. T. Eickemeyer, M. Kim, Y. J. Yoon, I. W. Choi, B. P. Darwich, S. J. Choi, Y. Jo, J. H. Lee, B. Walker, S. M. Zakeeruddin, L. Emsley, U. Rothlisberger, A. Hagfeldt, D. S. Kim, M. Grätzel, J. Y. Kim, *Nature* **2021**, 592, 381.
- [18] S. Paek, S. B. Khan, M. Franckevičius, R. Gegevičius, O. A. Syzgantseva, M. A. Syzgantseva, S. Kinch, A. M. Asiri, C. Roldán-Carmona, M. K. Nazeeruddin, *J. Mater. Chem. A* **2021**, 9, 5374.
- [19] X. Li, W. Zhang, X. Guo, C. Lu, J. Wei, J. Fang, *Science* **2022**, 375, 434.

- [20] Z. Xiong, L. Lan, Y. Wang, C. Lu, S. Qin, S. Chen, L. Zhou, C. Zhu, S. Li, L. Meng, K. Sun, Y. Li, *ACS Energy Lett.* **2021**, 6, 3824.
- [21] J. Peng, F. Kremer, D. Walter, Y. Wu, Y. Ji, T. Duong, H. Shen, T. Lu, F. Brink, C. Lem, J. Xiang, D. Zhong, L. Li, W. Liu, O. Lee, Y. Liu, K. J. Weber, T. P. White, K. R. Catchpole, *Nature* **2022**, 601, 573.
- [22] H. Min, D. Y. Lee, J. Kim, M. J. Paik, Y. K. Kim, G. Kim, K. S. Kim, K. S. Lee, J. Kim, M. G. Kim, T. J. Shin, S. I. Seok, *Nature* **2021**, 598, 444.
- [23] R. Guo, D. Han, W. Chen, L. Dai, K. Ji, Q. Xiong, S. Li, L. K. Reb, M. A. Scheel, S. Pratap, N. Li, S. Yin, T. Xiao, S. Liang, A. L. Oechsle, C. L. Weindl, M. Schwartzkopf, H. Ebert, P. Gao, K. Wang, M. Yuan, N. C. Greenham, S. D. Stranks, S. V. Roth, R. H. Friend, P. Müller-Buschbaum, *Nat. Energy* **2021**, 6, 977.
- [24] Y.-H. Lin, N. Sakai, P. Da, J. Wu, H. C. Sansom, A. J. Ramadan, S. Mahesh, J. Liu, R. D. J. Oliver, J. Lim¹, L. Aspitarte, K. Sharma, P. K. Madhu, A. B. Morales-Vilches, P. K. Nayak, S. Bai, F. Gao, C. R. M. Grovenor, M. B. Johnston, J. G. Labram, J. R. Durrant, J. M. Ball, B. Wenger, B. Stannowski, H. J. Snaith, *Science* **2020**, 369, 96.

- [25] J. Peng, Y. Wu, W. Ye, D. A. Jacobs, H. Shen, X. Fu, Y. Wan, T. Duong, N. Wu, C. Barugkin, H. T. Nguyen, D. Zhong, J. Li, T. Lu, Y. Liu, M. N. Lockrey, K. J. Weber, K. R. Catchpole, T. P. White, *Energy Environ. Sci.* **2017**, 10, 1792.
- [26] K. Domanski, B. Roose, T. Matsui, M. Saliba, S.-H. Turren-Cruz, J.-P. Correa-Baena, C. R. Carmona, G. Richardson, J. M. Foster, F. D. Angelis, h. J. M. Ball, A. Petrozza, N. Mine, M. K. Nazeeruddin, W. Tress, M. Graetzel, U. Steiner, A. Hagfeldt, A. Abate, *Energy Environ. Sci.* **2017**, 10, 604.
- [27] K. Deng, Q. Chen, L. Li, *Adv. Funct. Mater.* **2020**, 30, 2004209.
- [28] J. Wei, F. Guo, X. Wang, K. Xu, M. Lei, Y. Liang, Y. Zhao, D. Xu, *Adv. Mater.* **2018**, 30, 1805153.
- [29] S. Zhang, Z. Liu, W. Zhang, Z. Jiang, W. Chen, R. Chen, Y. Huang, Z. Yang, Y. Zhang, L. Han, W. Chen, *Adv. Energy Mater.* **2020**, 10, 2001610.
- [30] C. Altinkaya, E. Aydin, E. Ugur, F. H. Isikgor, A. S. Subbiah, M. D. Bastiani, J. Liu, A. Babayigit, T. G. Allen, F. Laquai, A. Yildiz, S. D. Wolf, *Adv. Mater.* **2021**, 33, 2005504.
- [31] B. L. Watson, N. Rolston, K. A. Bush, T. Leijtens, M. D. McGehee, R. H. Dauskardt, *ACS Appl. Mater. Interfaces* **2016**, 8, 25896.

- [32] K. Wojciechowski, I. Ramirez, T. Gorisse, O. Dautel, R. Dasari, N. Sakai, J. M. Hardigree, S. Song, S. Marder, M. Riede, G. Wantz, H. J. Snaith, *ACS Energy Lett.* **2016**, 1, 648.
- [33] C. Tian, G. Betancourt-Solis, Z. Nan, K. Liu, K. Lin, J. Lu, L. Xie, L. Echegoyen, Z. Wei, *Sci. Bull.* **2021**, 66, 339.
- [34] J.-L. Wang, X.-Q. Chen, X. Yao, S.-C. Wu, L.-N. Liu, W.-J. Xiao, H. Wang, J. Li, Z. Lu, W.-S. Li, *Tetrahedron Lett.* **2017**, 58, 2695.
- [35] Y. Bai, X. Yao, J. Wang, J.-L. Wang, S.-C. Wu, S.-P. Yang, W.-S. Li, *Tetrahedron* **2019**, 75, 4676.
- [36] K. Liu, C. Tian, Y. Liang, Y. Luo, L. Xie, Z. Wei, *Nano Research* **2022**, 15, 7139.
- [37] L. Krückemeier, B. Krogmeier, Z. Liu, U. Rau, T. Kirchartz, *Adv. Energy Mater.* **2021**, 11, 2003489.
- [38] M. Liu, A. Degterev, S. Dahlström, C. Ahläng, S. Wilken, A. Matuhina, M. Hadadian, M. Markkanen, K. Aitola, A. Kamppinen, J. Deska, O. Mangs, M. Nyman, P. D. Lund, J.-H. Smått, R. Österbacka, P. Vivo, *J. Mater. Chem. A* **2022**, 10, 11721.

- [39] O. Almora, C. Aranda, E. Mas-Marzá, G. Garcia-Belmonte, *Appl. Phys. Lett.* **2016**, 109, 173903.
- [40] Y. Liu, J. Sun, Z. Yang, D. Yang, X. Ren, H. Xu, Z. Yang, S. F. Liu, *Adv. Optical Mater.* **2016**, 4, 1829.
- [41] C. Ahläng, M. Nyman, R. Österbacka, *Phys. Rev. Applied* **2021**, 16, 014041.
- [42] Y. Yang, H. Lu, S. Feng, L. Yang, H. Dong, J. Wang, C. Tian, L. Li, H. Lu, J. Jeong, S. M. Zakeeruddin, Y. Liu, M. Grätzel, A. Hagfeldt, *Energy Environ. Sci.* **2021**, 14, 3447.
- [43] C. Ding, L. Yin, L. Zhang, R. Huang, S. Fan, Q. Luo, J. Lin, F. Li, C. Zhao, R. Österbacka, C.-Q. Ma, *Adv. Funct. Mater.* **2021**, 31, 2103820.
- [44] C. Ding, R. Huang, C. Ahläng, J. Lin, L. Zhang, D. Zhang, Q. Luo, F. Li, R. Österbacka, C.-Q. Ma, *J. Mater. Chem. A* **2021**, 9, 7575.
- [45] W. Tress, J. P. C. Baena, M. Saliba, A. Abate, M. Graetzel, *Adv. Energy Mater.* **2016**, 6.
- [46] M. A. Afroz, C. A. Aranda, N. K. Tailor, P. Y. Yukta, M. M. Tavakoli, M. Saliba, S. Satapathi, *ACS Energy Lett.* **2021**, 6, 3275.
- [47] H. Zhang, S. Zhao, F. Huang, *J. Mater. Chem. A* **2021**, 9, 27140.

[48] H. Qiu, J. Wan, J. Zhang, X. Wang, N. Zhang, R. Chen, Y. Xia, L. Huang, H.-L. Wang, *Adv. Sci.* **2021**, 8, 2101759.

[49] L. Yin, J. Cho, S. J. Kim, I. Jeon, I. Jeon, M. Park, M. Park, S.-Y. Jeong, D. H. Lee, D.-H. Seo, C.-R. Cho, *Adv. Mater.* **2021**, 33, 2104763.

Boosting Perovskite Solar Cells Efficiency and Stability: Interfacial Passivation of Crosslinked Fullerene Eliminates the “burn-in” Decay

Changzeng Ding, Li Yin, Jinlong Wang, Valentina Larini, Lianping Zhang, Rong Huang, Mathias Nyman, Liyi Zhao, Chun Zhao, Weishi Li, Qun Luo, Yanbin Shen, Ronald Österbacka, Giulia Grancini, Chang-Qi Ma**

In this paper, the Li⁺ ions migration induced “burn-in” degradation in n-i-p type PSCs was reported. To block the Li⁺ ion movement, a thin crosslinked PC₆₁BM (CL-PCBM) layer was introduced on top of the SnO₂ layer, resulting in Li⁺ immobilization. Finally, the efficiency and stability are largely improved.

